

We are IntechOpen, the world's leading publisher of Open Access books Built by scientists, for scientists

5,000

Open access books available

125,000

International authors and editors

140M

Downloads

Our authors are among the

154

Countries delivered to

TOP 1%

most cited scientists

12.2%

Contributors from top 500 universities



WEB OF SCIENCE™

Selection of our books indexed in the Book Citation Index
in Web of Science™ Core Collection (BKCI)

Interested in publishing with us?
Contact book.department@intechopen.com

Numbers displayed above are based on latest data collected.
For more information visit www.intechopen.com



OCT in Applications That Involve the Measurement of Large Dimensions

Nélida A. Russo, Eneas N. Morel, Jorge R. Torga and Ricardo Duchowicz

Abstract

The application of optical coherence tomography (OCT) technique is not very common when measuring large dimensions is required. This type of measurements can be critical to achieve satisfactory results in the manufacturing process of precision parts. Components and structures ranging from submillimeter to several centimeters size can be found in many fields including automotive, aerospace, semiconductor, and data storage industries to name a few. In this chapter, an interferometric system based on the swept source optical coherence tomography (SS-OCT) technique, which has a wide measurement range and good axial resolution, is presented and its constituent parts are analyzed. The scheme includes a self-calibration stage based on fiber Bragg gratings (FBGs) that allows monitoring the spectral position of the light source in each scan, having the advantage of being a passive system that requires no additional electronic devices. Several applications of the system are described, including measurement of distances up to 17 cm, characterization of multilayer transparent and semitransparent structures, simultaneous determination of thickness of the wall, internal and external diameter of glass ampoules or similar containers, thickness measurements in opaque samples or where the refractive index is unknown, etc.

Keywords: interferometry, optical coherence tomography, optical metrology, nondestructive testing, large axial range

1. Introduction

Optical coherence tomography (OCT) is a noninvasive, interferometric technique that provides real-time 3-D images with micrometric resolution and depth of penetration that can range from some millimeters to a few centimeters, depending on the technique employed and the material under study. OCT images provide structural information of a sample, based on backscattered light from different layers of material within it. This technique is considered the optical analogue to ultrasound; however, it achieves a higher resolution using near-infrared wavelengths, at the cost of decreasing depth of penetration.

OCT was developed in the early 1990s for the noninvasive imaging of biological tissue [1, 2]. The first application was in ophthalmology [3] where it has had great development [4–6], the same as in cardiology [7, 8], where commercial equipment

has already been developed. In biomedicine, the use of relatively long-wavelength light allows it to penetrate into the scattering medium.

In the last years, low-coherence interferometric techniques such as OCT have been proposed as a powerful tool for industrial nondestructive testing (NDT), even leading to the development of specific equipment. Among the industrial metrological applications, the following can be mentioned: the measurement of very thin thicknesses in semiconductor wafers [9, 10], the characterization of surfaces [11, 12], the control of thickness in the coating of pills in the pharmaceutical industry [13], and others. OCT systems based on fiber optics are particularly suitable for use in industrial [14], hostile (electromagnetic interference, radioactive, cryogenic, or very high temperatures) [15], or difficult-to-access environments [16]. Moreover, optical fiber-based OCT devices can take the advantage of beam stability and lower price of IR components used in optical communications. However, applications such as 3-D inspection in large parts (greater than a centimeter) constitute a little explored area, since its implementation still has some technological limitations [17]. When using time-domain OCT, the interference signal is generated from the displacement of a mirror in the reference arm of the interferometer to equalize the sample distances. For measuring great dimensions, it implies the use of very expensive, extremely accurate, and with high resolution moving mechanical systems. On the other hand, spectral or Fourier-domain OCT allows the design of an interferometric system more robust, compact, and faster [18], thereby increasing the mechanical stability and reducing the sensitivity to vibrations. However, since it uses a spectrometer to detect the interference signal, its spectral resolution limits the measuring range below 1 cm. The SS-OCT technique offers an interesting alternative provided by the use of tunable light sources [19–21] such as fiber-optic lasers with variable spacing Fabry-Perot filters or electro-optical modulators [22] or tunable semiconductor lasers by intracavity refractive index change or by the use of microelectromechanical system (MEMS) cavities [23]. In general, in these systems, it is possible to achieve a laser linewidth narrower than the resolutions typically obtained by a spectrometer. Consequently, the depth range, in this case given by the instantaneous linewidth of the laser (coherence length), can reach values in the order of 1 cm or more and greatly expand the potential industrial applications [24–28]. In this case, the detection system is a photodetector in conjunction with a digitizer or oscilloscope, simplifying the system. In general, scanning sources have the inherent problem of not being able to provide accurate information about the correspondence between the wavelength, the signal voltage applied to the tuning device, and the temporary location within each sweep [29]. Some solutions have been proposed [30, 31], but in general they are complex and expensive.

In this context, this chapter reports and discusses a simple and self-calibrated fiber-optic interferometric system based on the swept source optical coherence tomography (SS-OCT) technique, especially suitable when the measurement of large dimensions (several centimeters) is necessary as those ones involved in industrial metrological applications [32–37]. Its constituent parts are analyzed, and several applications are shown, including the measurement of several centimeter distances, characterization of multilayer structures, simultaneous determination of thickness of the wall, internal and external diameter of glass containers, thickness measurements in opaque samples (which allows the use of the system to perform profilometry of mechanical parts) or where the refractive index is unknown, etc. On the other hand, the use of a set of fiber Bragg gratings to relate the emission wavelength of the tunable laser source and the temporary position in each sweep is discussed. The factors that determine the resolution and the maximum range of distances to be measured are presented. It is shown that with this system it is possible to determine distances of up to 17 cm with a spatial resolution in the order

of 21 microns, which constitutes a very encouraging scheme for the dimensional inspection applications mentioned before.

2. Description of the measurement scheme

The measuring scheme used in this work is essentially composed of the stages or subsystems indicated in **Figure 1**. The light source, the self-calibration system, and the interferometric system used for the different applications were implemented using monomode optical fiber operating in the 1550 nm spectral region. In the following subsections, each of them will be discussed in detail.

Basically, an erbium-doped fiber laser tunable in the 1550 nm spectral region was used as the light source. It has sufficient coherence length to allow the formation of great depth images. A passive self-calibration stage based on fiber Bragg gratings allows counteracting the possible variation in the scanning speed of the laser caused by the tuner module, in addition to linking the emission wavelength of the laser and the temporal position in each sweep. The interferometric system consists of a Michelson-type arrangement for the measurement of distances and transparent object thickness or a ring interferometer with a Sagnac-Michelson configuration for the measurement of opaque samples (or with unknown refractive index). The temporal distribution of the interference signals was obtained using an InGaAs photodetector with 2 GHz bandwidth connected to a digital oscilloscope, although it can be replaced by any 200 MHz bandwidth DAC system and two acquisition channels. As will be explained in detail later, in order to carry out the processing of the detected signal while the light source sweeps in wavelength, the Fourier transform was applied, and the position of the interfering peaks allowed obtaining the desired distance or thickness.

2.1 Laser system

The light source was a continuous wave emission erbium-doped fiber laser, tunable in a spectral range from about 1520 to 1570 nm using a variable spaced Fabry-Perot filter (Micron Optics, FFP-TF2) that has a free spectral range (FSR) of 60 nm and a bandwidth of 60 pm. Sweeping is achieved by applying a periodical signal like a triangular voltage waveform to the filter cavity PZT actuator [38]. By varying the parameters (amplitude and offset) of this signal, it is possible to modify the tuning range of the fiber laser and consequently the value of the maximum measurable distance. The sweep frequency could be varied up to 100 Hz. The erbium-doped fiber was pumped by a semiconductor laser diode emitting at 980 nm. The length of the doped fiber was selected taking into account a trade-off between spectral emission flatness and output power. The fiber laser output beam was extracted from the ring cavity through the 10% port of a 10/90 optical coupler. **Figure 2** shows the laser emission as it sweeps the tuning range, recorded by an optical spectrum analyzer (OSA) (Yokogawa, model AQ6370B). Since the acquisition speed of this instrument is much slower than the speed at which the F-P filter can be moved, the OSA records several sweeps of the laser finding it in different

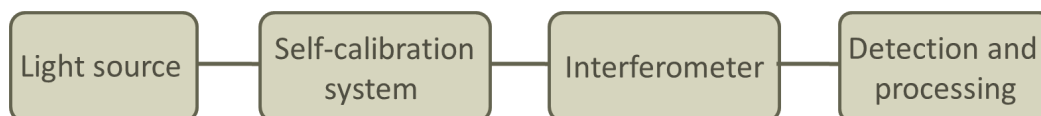


Figure 1.
Block diagram of the measuring system.

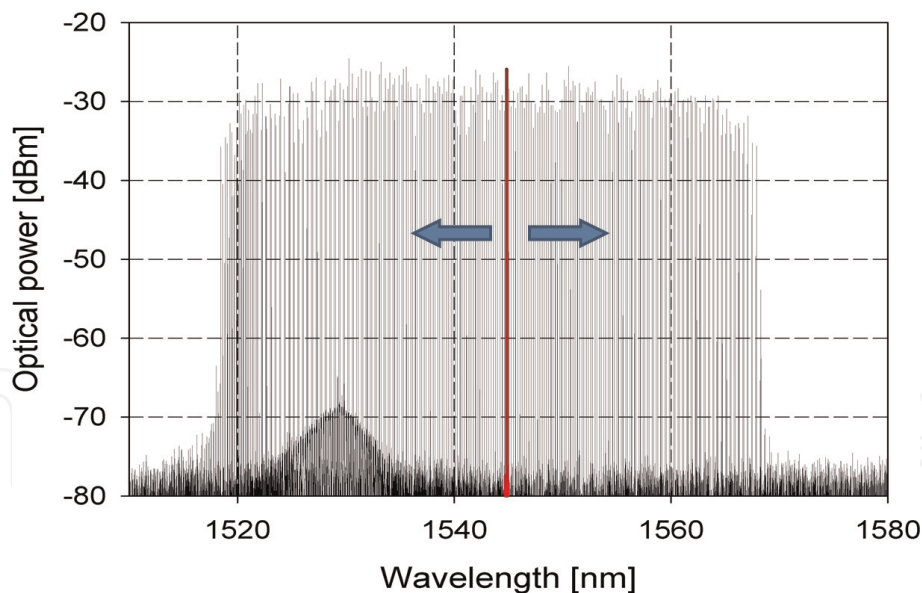


Figure 2.
Scanning spectrum of the laser source.

spectral positions. One of them is highlighted and the arrows represent the sweeping of the emission. As can be seen, despite the relatively low output power, the fiber laser has a very good S/N ratio. When the laser operates at any fixed wavelength within the tuning range, the emission spectrum has a typical width of 20 pm at 3 dB.

By considering a rectangular spectral profile when the laser source is tuned in the abovementioned range, the maximum theoretical axial resolution (or depth resolution) of the measurement system can reach 21 μm , which is derived from the following expression (Eq. (1)):

$$Res = \frac{2 \ln(2)}{\pi} \frac{\lambda_0^2}{\Delta\lambda} \quad (1)$$

where λ_0 is the central wavelength of the source spectrum and $\Delta\lambda$ is the spectral width of the broadband light source or, in our case, we should consider the tuning range. However, depending on the requirements, it is possible to modify (decrease) the swept range by means of the FP filter controller, which obviously worsens the axial resolution.

2.2 Calibration of the laser emission

In applications of low-coherence interferometry by swept source, the linear sampling process of spatial frequency (k -space) is critical. In the system used in this work, the tuning of the laser is done by controlling the cavity of a Fabry-Perot filter, by applying a triangular signal to a piezoelectric actuator. This process is affected by different factors such as hysteresis of the piezoelectric actuator (PZT) and errors in the repetition control of the scan cycle, which may make the spectral position of the laser emission unknown at each instant of time. Thus, the use of a self-calibration system is proposed [32, 33], which consists of a set of fiber Bragg gratings (FBGs) [39–41] centered on different wavelengths within the tuning range of the light source. This has the advantage of being a passive system, which does not require additional electronic devices. This system allows relating the emission wavelength of the source and the temporal position in each sweep. Since the spectral locations of the FBGs are known, from the measurement of their temporal positions, it is

possible to calibrate the OCT measurement system, resizing for each sweep of the source the time axis provided by the oscilloscope used to acquire the signal. The objective is to obtain a sequence of values k_{FBG_i} (wave number corresponding to the i^{th} filter) and the associated times (t_{FBG_i}) within the whole scanning range. In this way, two vectors k_{FBG_i} and t_{FBG_i} can be generated (Eqs. (2) and (3)):

$$k_{FBG} = [k_{FBG_1}, k_{FBG_2}, k_{FBG_3}, \dots, k_{FBG_n}] \quad (2)$$

$$t_{FBG} = [t_{FBG_1}, t_{FBG_2}, t_{FBG_3}, \dots, t_{FBG_n}] \quad (3)$$

With these values of t_{FBG} and k_{FBG} , a curve is obtained that represents the nonlinearity in the movement of PZT. From an interpolation, we obtain the function $k(t)$ that relates the sampling times to a uniformly sampled k -space, and from it we obtain the sampling frequency to be used in the calculation of the Fourier transform (Eq.(4)):

$$f_s = \frac{1}{(k_{n-1} - k_n)} \quad (4)$$

The error of the frequency f_s is obtained from the propagation of errors in the following way:

$$\Delta f_s = \left| \frac{\partial f_s}{\partial \Delta k} \right| \Delta k \quad (5)$$

In principle, the number of FBGs to use is a trade-off between obtaining the best calibration curve to minimize adjustment errors and generating the least possible deterioration in the detected signal due to insertion losses and noise caused by backward reflections.

As it is known, FBGs are sensitive to thermal changes, so variations in the temperature of the environment induce changes in their spectral positions. However, since all the gratings that integrate our calibration system are recorded in the same type of optical fiber and all of them experience the same temperature change, this will not generate measurement errors of the OCT system. This is because to determine the value of the sampling frequency, it is only relevant that the value Δk between FBGs remains constant, even though their individual positions (k_i) may change. The change in the absolute spectral positions of the Bragg gratings due to thermal variations only generates a shift in the k -space and does not affect the determination of the sampling frequency. On the other hand, gratings do not need to be equally spaced within the range of laser tuning. The central wavelengths of the FBGs employed in our work were 1527.84, 1535.73, 1541.82, 1547.65, 1553.62, and 1558.43 nm, and their spectral widths were in the order of 0.1 nm.

2.3 Fiber-optic interferometric system

2.3.1 Michelson interferometer

The configuration used for the measurement of distances or thicknesses of transparent samples consists of a Michelson-type interferometric system that is shown schematically in **Figure 3**.

If the light source has a spectral profile $S(k)$ and considering the interaction between the reference arm (RA) and the first interface (L_1) of the sample arm (SA), the interference signal is determined by

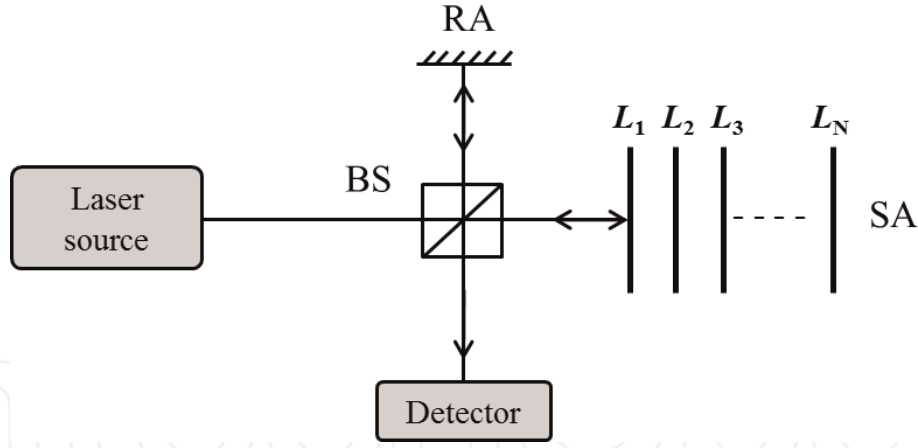


Figure 3. Basic configuration of the Michelson-type interferometer. BS, beam splitter; RA, reference arm; SA, sample arm; $L_1 \dots L_N$, different interfaces of the sample.

$$I(k) = S(k) \left[I_r + I_{L_1} + 2\sqrt{I_r I_{L_1}} \cos(k(d_r - d_{L_1})) \right] \quad (6)$$

where $d_r - d_{L_1} = n \Delta d$ is the optical path difference (OPD) that light travels between the RA and the L_1 interface of the sample and n is the group refractive index of the medium. It is evident that the cosine frequency indicates the value of $n \Delta d$. This type of signal is obtained when the system is used to measure the distance to an opaque surface.

If a sample with multiple interfaces (L_1 to L_N) is considered, the multiple reflections that appear will generate different terms or interference components, and the total intensity can be described by the following equation:

$$I(k) = S(k) \left[I_r + \sum_{n=1}^N I_{L_n} + \sum_{n=1}^N 2\sqrt{I_r I_{L_n}} \cos(k(d_r - d_{L_n})) \right. \\ \left. + \sum_{n \neq m=1}^N 2\sqrt{I_{L_n} I_{L_m}} \cos(k(d_{L_m} - d_{L_n})) \right] \quad (7)$$

The first term of Eq. (7) is the intensity reflected in the mirror of the reference arm, and the second is the sum of the intensities reflected in the different interfaces of the sample. These two terms are often referred to as “constant” or “DC” components. The first one generates the largest contribution to the detected intensity if the reflectivity of the reference dominates over the reflectivity of the different layers of the sample. The second sum is called “cross-correlation” for each reflector of the sample, and it depends on both the wave number of the light source and the OPD between the reference arm and the reflector considered in the sample arm. These terms are usually smaller than the DC part. However, the dependence of the square root represents an important logarithmic gain factor over the direct detection of the reflections of the sample. The third sum is called “autocorrelation” and represents the interference that occurs between the different interfaces present in the sample. Since the autocorrelation terms depend linearly on the reflectivity of each layer of the sample which cannot be controlled, a way to manage their intensities is the appropriate selection of the reference reflectivity. In the last two sums, the direct interactions of each interface with the reference arm ($d_r - d_{L_n}$) and the additional

interactions between the different interfaces of the medium to be analyzed ($d_{Lm}-d_{Ln}$) are evident. It should be clarified that in this case the different OPDs can be linked to different refractive index depending on the medium through which the light propagates. Then, it is necessary to consider the refractive index that corresponds to each layer.

As regards the fiber-optic implementation of the aforementioned interferometric system, two variants were used, which can be seen in **Figure 4**. In the case of distance measurement, the light beam is divided by a fiber-optic coupler (FC 50/50). One of the beams is directed to the reference surface (a mirror) and the other to the sample. After being reflected in each of these surfaces, both beams are directed to the detection system, where their superposition generates the interference signal. From its processing, the optical path difference (OPD) between both arms is obtained and, consequently, the unknown distance. When it is desired to measure transparent or semitransparent samples, light is reflected from subsurface structures within it (e.g., from both sides of the sample if its thickness is being measured or from the different interfaces if it is a multilayer sample), so it is possible to perform a tomography measurement.

2.3.2 Sagnac-Michelson interferometer

For the measurement of opaque samples, it is necessary to modify the interferometric system and use a configuration based on a combination of the Michelson interferometer with the Sagnac interferometer. This configuration allows the determination of thicknesses of opaque samples or whose refractive index is unknown, as well as the surface characterization of nontransparent objects (profilometry of mechanical parts).

Figure 5 shows the configuration of the Sagnac-Michelson interferometer in optical fiber, where E1 is the mirror of the reference arm, while BS1 and BS2 are beam splitters implemented with fused fiber-optic couplers with a coupling ratio 50:50. The beams that illuminate both the mirror in the reference arm and both sides of the sample are collimated by means of two single-mode GRIN fiber-optic collimators (Col.). The ring that forms at the output of BS2 with the beams that illuminate the sample forms the Sagnac configuration.

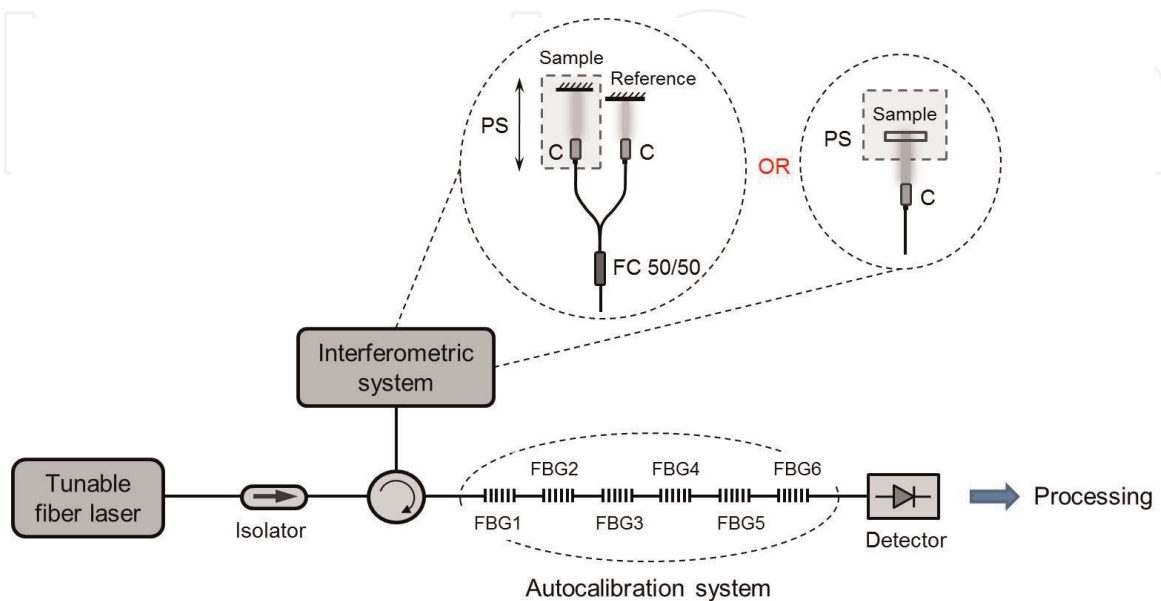


Figure 4.
 Detailed setup employed to measure distances and thicknesses of multilayer transparent samples. PS, positioning system; C, collimator; FC, fiber coupler.

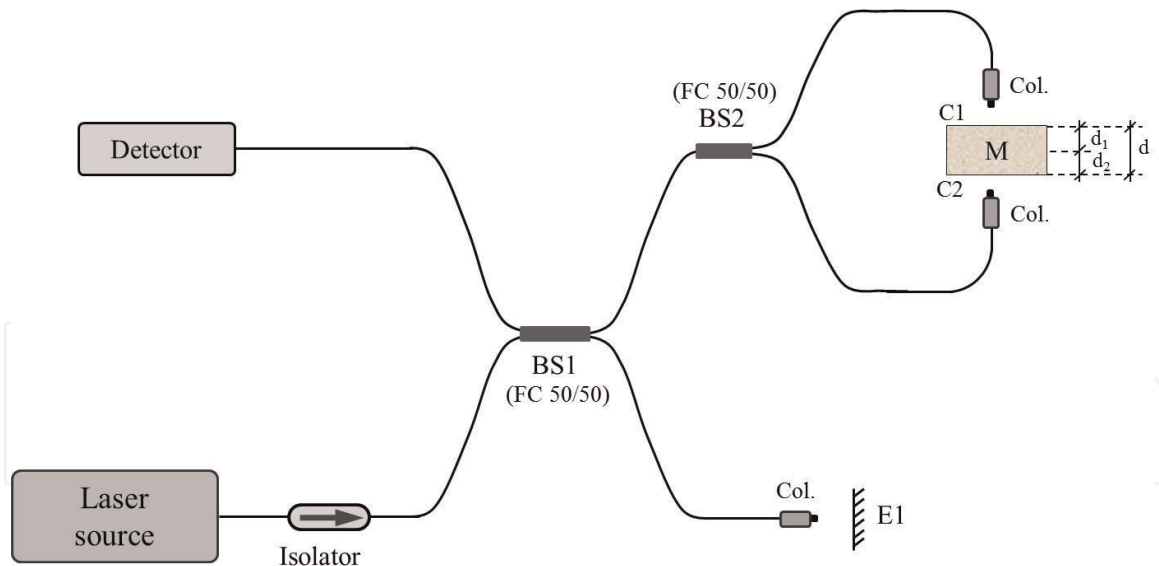


Figure 5.
Sagnac-Michelson interferometer implemented in optical fiber.

The path performed by the light beam can be described as follows. After the first splitter (BS1), one beam travels toward the reference (E1) and the other toward the second splitter (BS2), where it is separated again into two beams, each of which illuminates opposite faces of the sample. Upon reaching the sample (M), the beams are reflected and perform the reverse way. The reflections on the three surfaces, the mirror E1 and the two faces of the sample C1 and C2, are superimposed on the detector and produce the interference signal containing the information of interest (the thickness of the sample in the direction of illumination).

The optical path differences between the distances traveled by the different light beams generate the modulations in the interference signal, which are analyzed in the Fourier space. From this analysis, the OPDs can be determined in each case, obtaining the position of the maximum of the “interference peak” in the Fourier transform.

We will call P_r as the position (in the OPD axis) of the peak corresponding to the term (or component) of the interference signal generated by the reflection at E1 (reference beam) and the beam traveling through the Sagnac interferometer when there is no sample (and with the corresponding collimators aligned); P_1 as the peak that is produced by the interference between the reference and the reflection on the face C1 of the sample; P_2 as the interference peak that occurs between the reference and the reflection on the other side of the sample (C2). The distances L_i represent the paths traveled by the light in the different sectors of the interferometer (see **Figure 5**), that is, L_1 is the optical path between BS2 and the face C1 of the sample, L_2 is the optical path between BS2 and the face C2 of the sample, L_3 is the optical path between BS1 and BS2, LR is the length of the reference arm (between BS1 and E1), and d is the thickness of the sample. In addition, d_1 and d_2 are the segments of the thickness of the sample (d) on each side of the axis of symmetry of the Sagnac interferometer. Therefore,

$$d = d_1 + d_2 \quad (8)$$

$$P_r = 2LR - (2L_3 + L_1 + L_2 + d) \quad (9)$$

$$P_1 = 2LR - 2(L_3 + L_1) \quad (10)$$

$$P_2 = 2LR - 2(L_3 + L_2) \quad (11)$$

By operating with the above equations, it is possible to determine the thickness of the sample from

$$(P_1 + P_2) - 2P_r = 2d \quad (12)$$

From this last expression, it is possible to determine the thickness of the sample under study. It is interesting to note that it was not necessary to make considerations regarding the lengths that the interferometer branches should have or the position of the sample so that Eq. (12) is general and can be used in any condition.

2.4 Detection and processing

The temporal distribution of the optical intensity corresponding to the interference signal was obtained using an InGaAs photodetector connected to a digital oscilloscope. **Figure 6** shows a typical record of (a) a triangular voltage signal used to tune the fiber laser, (b) an interferometric signal that contains the dimensional information of the sample, and (c) the calibration signal with FBG attenuation peaks used to relate the emission wavelength of the source and the temporal position in each sweep.

Basically, the Fourier transform was then applied to the detected signal, and the position of the interference peak allowed obtaining the desired distance or thickness. As was mentioned before, the interference signal is affected by uncertainties that arise from the nonlinear movement of the PZT used to sweep the laser. To overcome this problem, fiber Bragg gratings of known spectral positions were used, which allowed transforming the temporal axis into an axis in wave number (k). To apply the fast Fourier transform (FFT) that reconstructs the axial scan as a function of depth, the spectrum must be sampled uniformly in the k -space. Therefore, a linearization of the k -vector was performed, and the interference signal was interpolated to obtain a sampled signal at equally spaced intervals. The resampled interference signal can be expressed as indicated in Eq. (13):

$$I(k) = S(k) \left[I_1 + I_2 + 2 \sqrt{I_1 I_2} \cos(k(nd)) \right] \quad (13)$$

where k is the wave number, $S(k)$ is the spectral profile of the light source, I_1 and I_2 are the amplitudes of the intensities reflected in both arms of the interferometer (to simplify the notation, their dependence with k was not indicated), and nd is the optical path difference (with n being the group refractive index of the medium in which light is propagated and d being the difference in length between both interferometer arms).

To illustrate the procedure used, the graphs obtained by measuring a thickness of $d = 500$ microns and $n = 1$ are shown. In that case, the interference signal in the k -space has the shape shown in **Figure 7**.

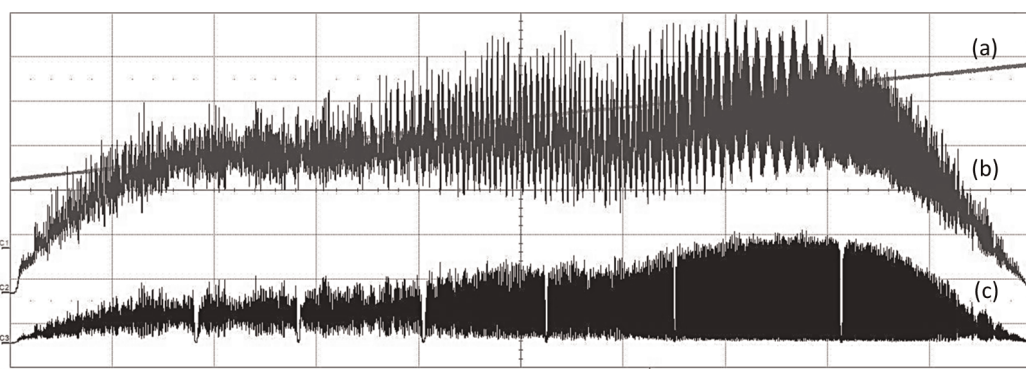


Figure 6.
 Typical records obtained with an oscilloscope when measuring the thickness of a sample.

The Fourier transform of this signal can be expressed as indicated in Eq. (14), where it can be seen that the spectral profile of the light source is convolved with the deltas coming from the DC term and the interfering term of Eq. (13):

$$I(x) = S(x) \otimes [\delta(x) + \delta(x \pm (n d))] \quad (14)$$

Then, the signal was passed through a high-pass filter that eliminates the DC component, obtaining a signal as indicated in **Figure 8**, which can be expressed as

$$I'(k) = S(k) 2\sqrt{I_1 I_2} \cos(k(n d)) \quad (15)$$

It is evident that the amplitude depends on the spectral profile of the light source ($S(k)$) and it is desirable to eliminate this dependence. For this, the Hilbert transform [42, 43] is used, which gives a quadrature signal (Eq. (16)), that is

$$\tilde{I}'(k) = S(k) 2\sqrt{I_1 I_2} \sin(k(nd)) \quad (16)$$

By making the square sum of both, Eq. (17) is obtained:

$$\left(S(k) 2\sqrt{I_1 I_2} \sin(k(nd)) \right)^2 + \left(S(k) 2\sqrt{I_1 I_2} \cos(k(nd)) \right)^2 = \left(S(k) 2\sqrt{I_1 I_2} \right)^2 \quad (17)$$

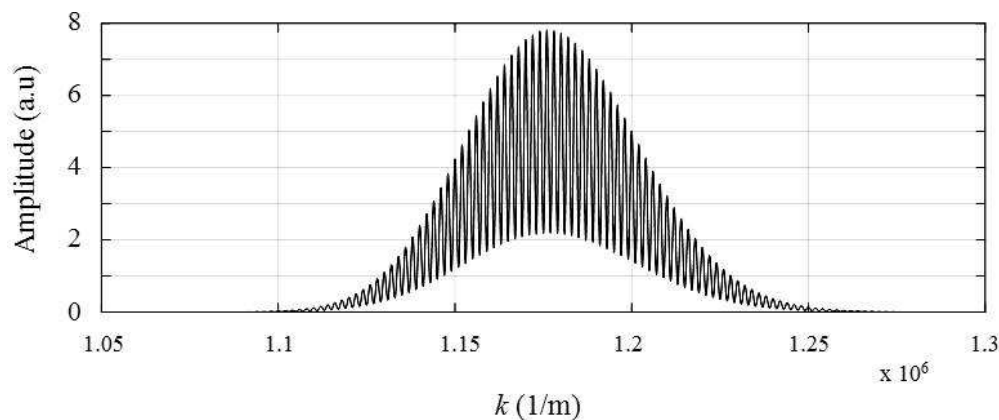


Figure 7.
Interference signal $I(k)$.

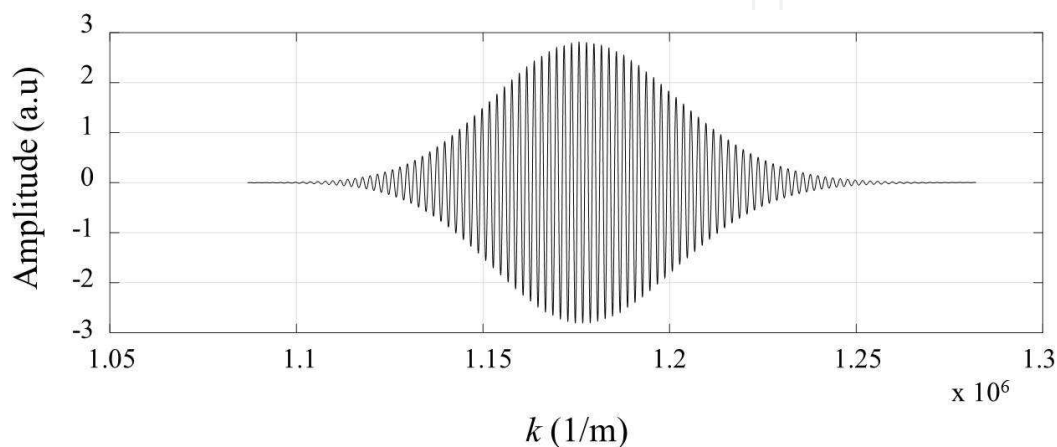


Figure 8.
Interference signal after the high-pass filter.

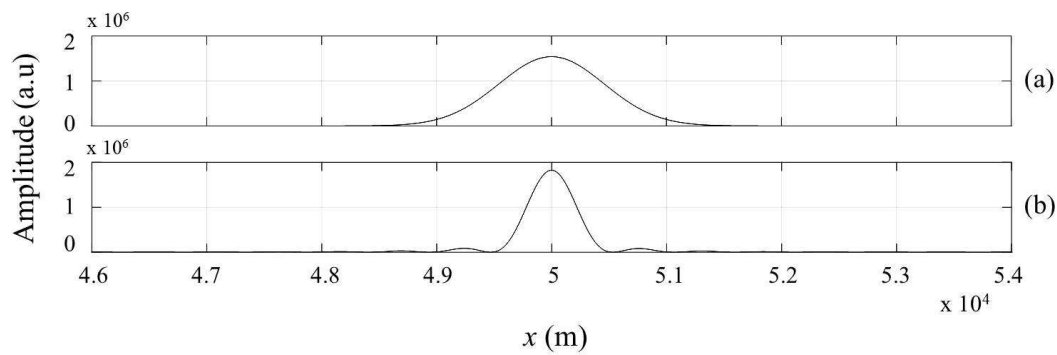


Figure 9.
 Fourier transforms of (a) $I'(k)$ and (b) $I''(k)$.

Then, just by calculating the square root of the sum of the squares of the real and imaginary parts, it is possible to eliminate the spectrum of the light source (Eq. (18)):

$$\frac{I'(k)}{S(k) 2 \sqrt{I_1 I_2}} = \cos(k(nd)) \quad (18)$$

When using this simple method to obtain $S(k)$, there is a problem if it presents zero crossings, which would cause the signal to tend to infinity and produce unwanted results. To avoid this, a constant ξ is usually added to the denominator of the previous expression (Eq. (19)):

$$I''(k) = \frac{I'(k)}{(S(k) 2 \sqrt{I_1 I_2} + \xi)} = \cos(k(nd)) \quad (19)$$

Based on this improvement, it is possible to reduce the width at half height by $\sim 40\%$, improving the uncertainty in detecting the position of the maximum at the peak of the Fourier transform. This improvement is exemplified in **Figure 9**, where graph (a) shows the shape of the peak without performing the Hilbert transform and graph (b) after applying that transform.

Finally, and to improve the S/N ratio, the autocorrelation of $I''(k)$ is performed.

3. Measurements with the OCT system

In this section, different experimental results that demonstrate the potential of the proposed scheme for quality control in industrial applications will be presented [32, 33].

3.1 Long-distance measurements

To apply the proposed system to long-distance measurement, a Michelson-type interferometer was mounted as shown in **Figure 10**. The illumination beam was divided by a 50:50 single-mode fiber coupler, and its outputs were collimated to impinge both on the sample (moving mirror M1) and on the mirror of the reference arm (M2). In order to determine the measuring range of the system, the sample mirror was mounted on a rod with preset positions separated 5 cm, while the reference mirror was placed on a translation stage with a micrometric screw of 5 cm travel. Then, by combining the displacements of both mirrors, it was possible to

obtain a continuous variation of the distance to be measured, reaching a possible measuring range of about 20 cm.

Several distances within the measuring range were determined, and it was verified that the system was able to measure up to 17.24 cm. When processing the interference signals using the Hilbert-Fourier transform, it was observed that the peaks lost intensity as the OPD increased. This was due to the divergence of the collimators used in the setup and the coherence length of the light source. The drop in the visibility of the processed signal can be observed in **Figure 11** where, as the

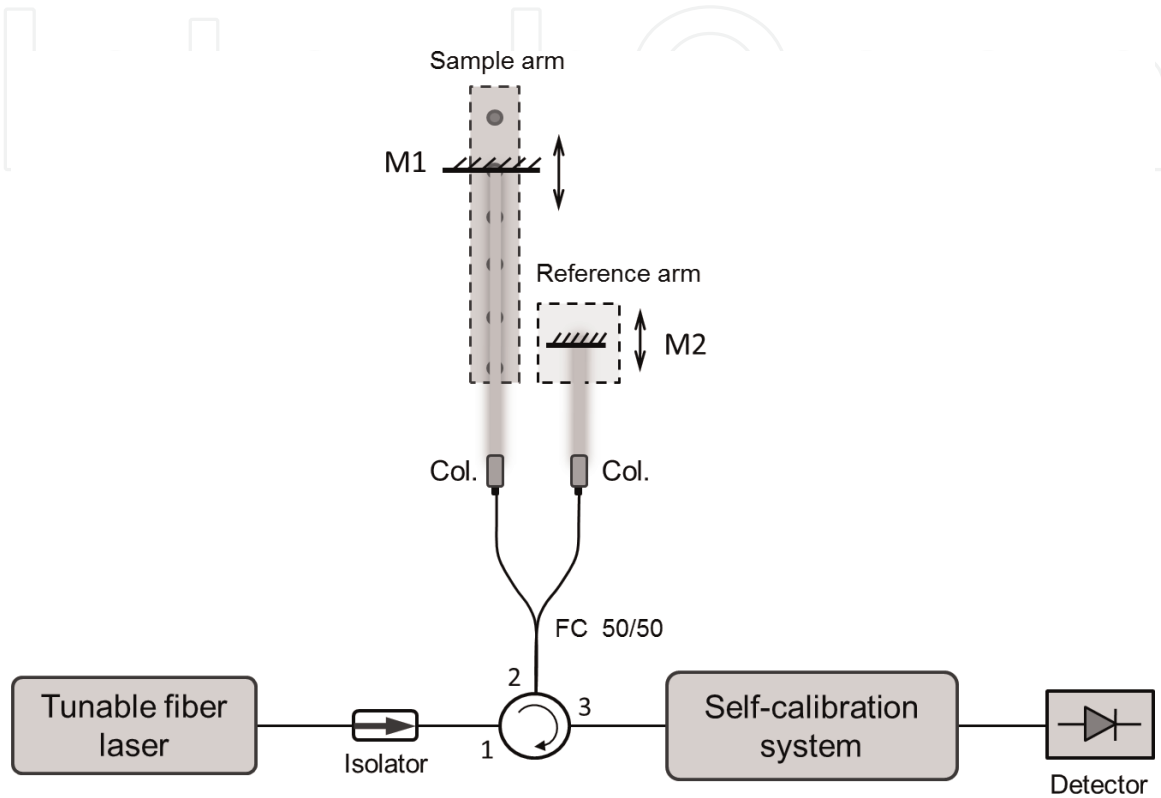


Figure 10.
Experimental setup for long-distance measurement.

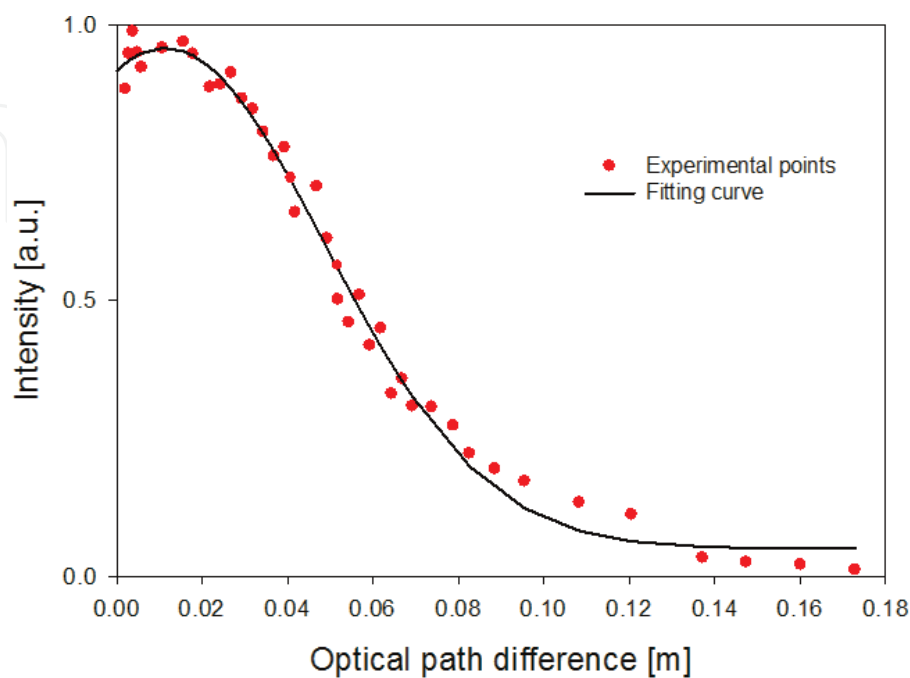


Figure 11.
Normalized amplitude of the Fourier peaks corresponding to different OPDs.

OPD grows, the amplitude of the interference peak decreases, which produces the degradation of the signal-to-noise ratio and limits the maximum measurable distance to the value previously mentioned.

The measurement depth, that is, the theoretical maximum distance that the system can measure (Δz_{max}), is determined by

$$\Delta z_{max} = \frac{\lambda_0^2}{4 n_g \delta_\lambda} \quad (20)$$

where λ_0 is the central wavelength of the source spectrum, n_g is the group refractive index of the medium in which light is propagated, and δ_λ is the spectral width of the tunable laser when it is sweeping in wavelength (somewhat larger than that corresponding to the emission at any fixed wavelength within the tuning range). For the tunable laser source used in our measuring system, it can be considered $\delta_\lambda = 30$ pm, so, theoretically, $\Delta z_{max} = 20$ cm. However, it was experimentally verified that the aforementioned drop in visibility slightly reduced this value to just over 17 cm.

3.2 Measurement of multilayer transparent samples

The system described in this chapter was used to measure the thickness of the walls and distance between them for different transparent and semitransparent containers, of different sizes, colors, and shapes, as well as to dimensionally characterize multilayer transparent objects in order to expand the possible applications.

The setup used corresponds to a single-arm Michelson interferometer. In this type of configuration, the interference signal is obtained from the superposition of the reflections in each of the interfaces present in the sample, which makes it possible to eliminate errors due to reference vibrations and a better use of the light source. Initially, measurements were made on rectangular glass cuvettes and on round glass containers (e.g., ampoules and jars used in the pharmaceutical industry and glass bottles used in the beverage industry), seeking to determine the thicknesses of the walls, the internal and external dimensions or diameters, and the shape in each one. In order to measure cylindrical containers, the samples were mounted on a rotating platform that allows measurements to be taken in different sectors. This type of measurements can be used to perform quality control during the manufacturing process of such containers. In **Figure 12**, a glass jar or cuvette is shown schematically, as well as the dimensions to be measured and the beams reflected in the different interfaces.

If we consider the beams reflected in each interface of the container, 6 interference signals will be generated that will give rise to the corresponding Fourier transform peaks, from which it will be possible to obtain the information of the dimensional parameters of the mentioned container (**Figure 13**). If we call $P_{m,n}$ the position on the OPD axis of the Fourier transform peak corresponding to the interference signal generated by the reflections I_m and I_n and n_i the refractive index of the layer (i) of thickness T_i , then the position of the peak can be expressed as

$$P_{m,n} = \sum_{k=m}^{n-1} T_k n_k \quad (21)$$

If we consider the glass container shown in **Figure 12**, the refractive indexes will be those of glass and air (n_g and $n_a = 1$, respectively), then

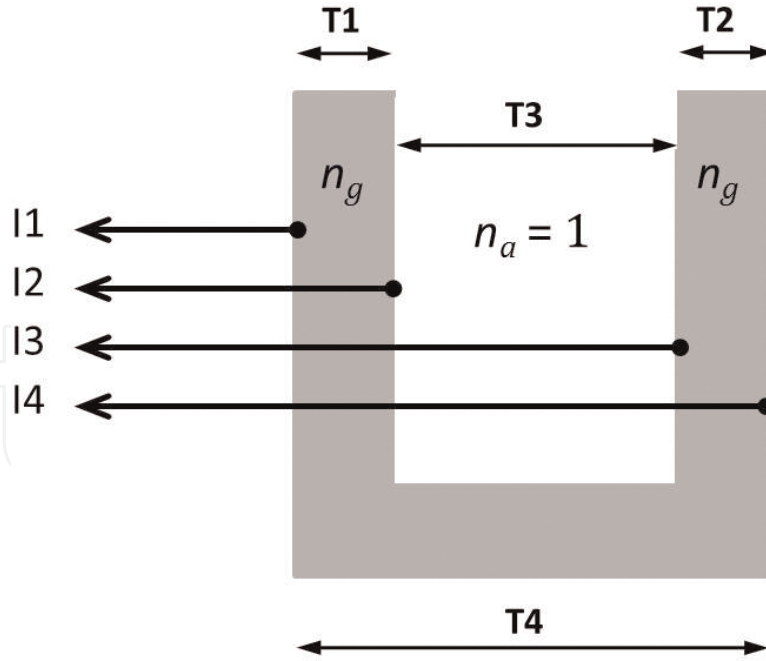


Figure 12. Generic scheme of a container showing the beams reflected on each interface and the dimensions to be measured.

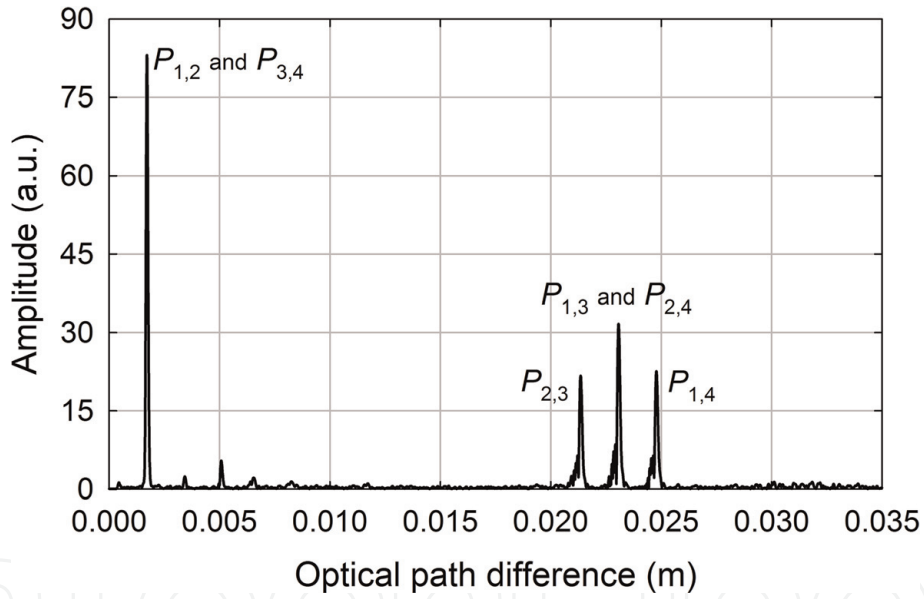


Figure 13. Fourier transform of the interference signal obtained when measuring a small glass bottle.

$$P_{1,2} = T_1 n_g \quad (22)$$

$$P_{3,4} = T_2 n_g \quad (23)$$

$$P_{2,3} = T_3 \quad (24)$$

$$P_{1,3} = T_1 n_g + T_3 \quad (25)$$

$$P_{2,4} = T_3 + T_2 n_g \quad (26)$$

$$P_{1,4} = T_1 n_g + T_3 + T_2 n_g \quad (27)$$

From these equations it is possible to obtain the dimensions of the container as

$$T_1 = \frac{P_{1,2}}{n_g} \quad (28)$$

$$T_2 = \frac{P_{3,4}}{n_g} \quad (29)$$

$$T_3 = P_{2,3} \quad (30)$$

$$T_4 = P_{2,3} + \frac{(P_{1,2} + P_{3,4})}{n_g} \quad (31)$$

As an example of the different measurements made in this type of samples, **Figure 13** shows results obtained when measuring a small glass bottle.

As can be seen, $P_{1,2}$ was superimposed with $P_{3,4}$, so both thicknesses were equal $T_1 = T_2 = 1.15$ mm; the distance between the walls of the bottle (or internal diameter) arises from $P_{2,3}$ and resulted in $T_3 = 21.3$ mm, while $P_{1,4}$ provides information on the external size (or diameter) of the container, resulting in $T_4 = 23.6$ mm. The peak $P_{1,3}$ coincides with $P_{2,4}$ and comes from the interference between the reflected beam on one of the internal walls and the opposite outer one. **Table 1** summarizes the values obtained after a complete rotation of the same glass bottle.

Other samples like glass ampoules, jars, and beakers like those used in laboratory up to 5 cm external diameter were measured.

Subsequently, in order to expand the possible applications of the developed system, different multilayer samples formed by glass plates separated by layers of air were measured. The objective was to determine the thickness of each of the different layers as well as the total dimensions of the sample. This type of measurement would allow, for example, the determination of the thickness of internal partitions in containers, helping to carry out quality control during the manufacturing processes. Two samples were measured, one consisting of three glass thicknesses and two air thicknesses, and another formed by four glass walls separated by three air spaces. The latter is schematized in **Figure 14**, where the thicknesses of the different layers (G_i and A_i) are indicated, as well as the intensities reflected in the different interfaces (I_i). In this configuration, eight reflections are produced and combined to generate the different peaks in the Fourier transform of the interference signal. **Figure 15** shows the experimental result obtained when measuring this multilayer object. There, only those peaks that provide relevant information to directly determine the searched dimensions were labeled. The other peaks correspond to different combinations between the thicknesses analyzed. Besides, higher amplitude peaks indicate that for this sample there is more than one interface with the same thickness. Simulations performed with the values of the

Angular position	$T_1 = T_2$ (m)	T_3 (m)	T_4 (m)
0°	0.001178	0.021273	0.023598
45°	0.001146	0.021313	0.023601
90°	0.001178	0.021301	0.023644
135°	0.001142	0.021352	0.023639
180°	0.001179	0.021316	0.023642
225°	0.001138	0.021358	0.023656
270°	0.001168	0.021334	0.023675
315°	0.001143	0.021271	0.023554
360°	0.001143	0.021271	0.023554

Table 1. Measurement of thicknesses (T_1 and T_2) and internal (T_3) and external (T_4) diameters of a small glass bottle when rotating on its axis of symmetry.

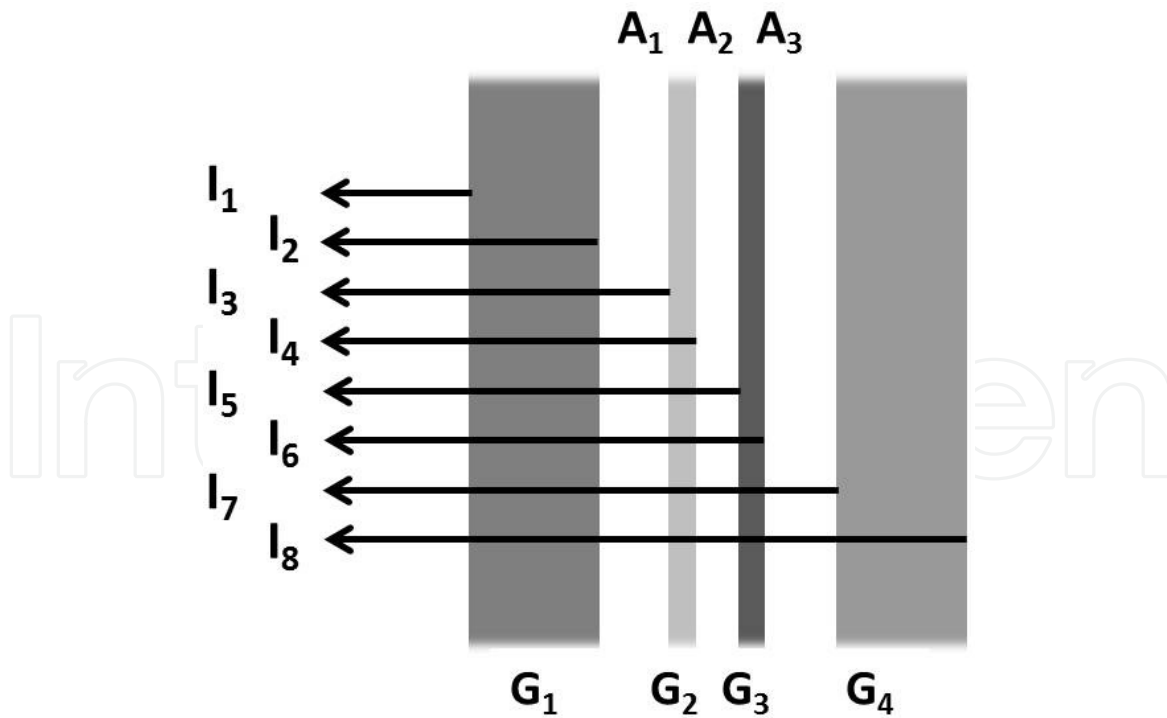


Figure 14.
Multilayer sample consisting of four glass walls separated by layers of air.

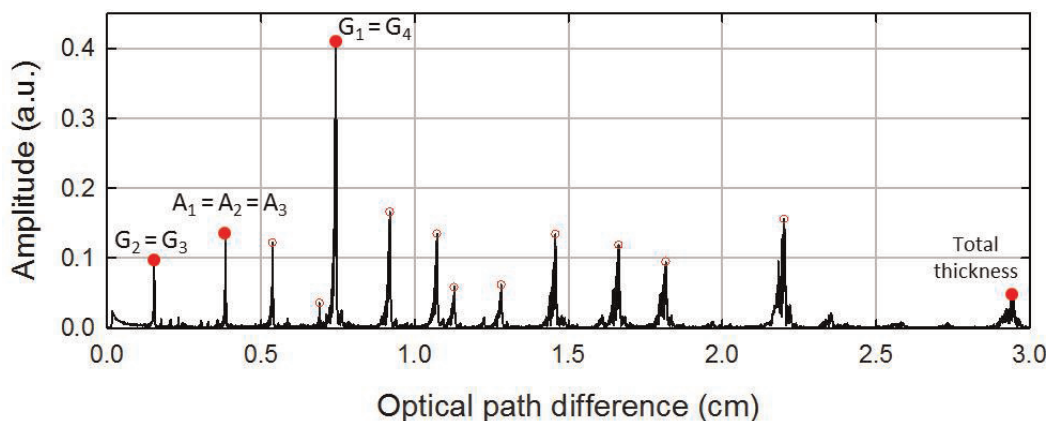


Figure 15.
FFT of the interference signal obtained when measuring a sample of seven layers.

thicknesses mechanically measured showed the same number of interference peaks located in the same spatial positions, so it is evident that this system is capable of characterizing large multilayer samples.

3.3 Measurement of opaque objects

As discussed in Section 2.3.2, the interferometric system was slightly modified to measure opaque samples. The configuration used is shown schematically in **Figure 16**.

Eight opaque samples (aluminum cylinders) of different thicknesses between 5 and 50 mm were measured. For each of the samples, the following were recorded: (1) the interferometric signal obtained with the reference and the Sagnac ring without the object and (2) the interferometric signal with the object placed inside the Sagnac ring and the reference. This allows to obtain the OPDs corresponding to the peaks P_r , P_1 , and P_2 of Eq. (12) from which it is possible to determine the

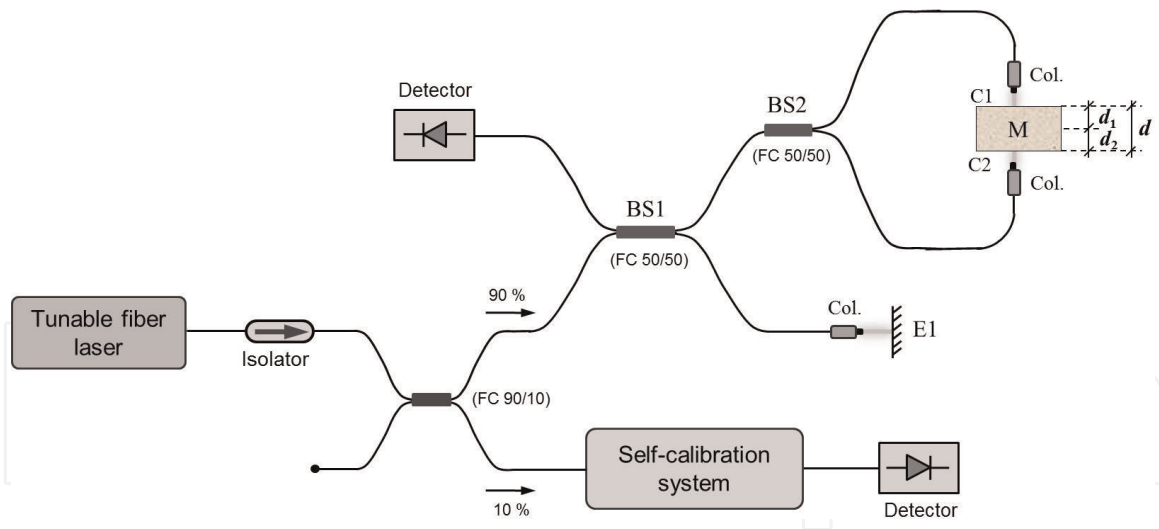


Figure 16.
 Experimental setup used to measure opaque samples.

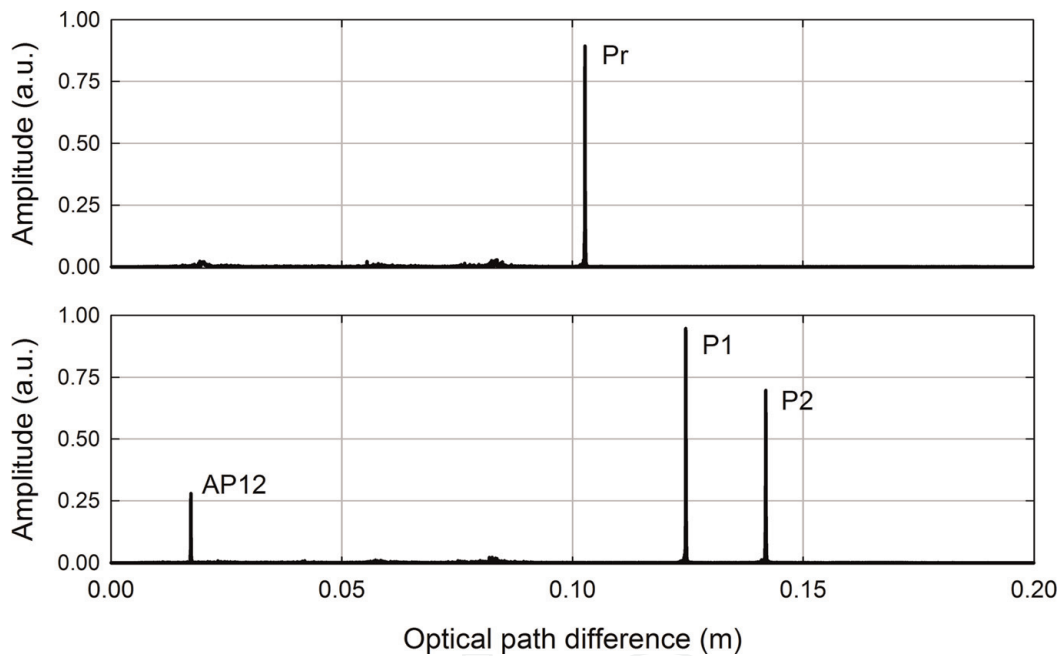


Figure 17.
 Fourier transform of the interference signal obtained when measuring an opaque sample of 30.44 mm thickness.

thickness d of the object as explained in Section 2.3.2. In **Figure 17**, the Fourier transforms corresponding to both situations for one of the samples are observed, resulting in a thickness $d = 30.44$ mm. The AP12 peak always appears in this type of measurements and is the OPD between each of the faces of the sample, that is, it corresponds to the interference signal between the reflections on both sides of the object, although it is not taken into account to determine its thickness.

4. Conclusions

This chapter discusses the development of a simple, self-calibrated system, based on the SS-OCT technique, and its metrological applications in nonmedical areas where the determination of large dimensions (several centimeters) is required. This type of measurement is of great interest, for example, to carry out quality control in manufacturing processes. The developed system allows not only

tomography of transparent or semitransparent multilayer samples but also the measurement of thicknesses of opaque mechanical parts. The implemented scheme allowed to measure distances somewhat greater than 17 cm with an axial resolution of 21 μm , which extends the measurement range obtainable with the usual OCT schemes while maintaining a good axial resolution. This is important for applications in areas of metrology and nondestructive testing in the industrial field. The system uses a laser source of ~ 20 pm bandwidth tunable in the spectral region of 1550 nm, which has sufficiently long coherence length to enable long depth range imaging. The design includes an online, passive self-calibration stage implemented with a set of fiber Bragg gratings. The calibration system provides the correspondence between the wavelength and the temporary location of the laser emission within each sweep, which allows to correct, in a simple way and without additional electronic devices, possible indeterminations in the relation between both parameters. It was verified that the possible temperature changes do not affect the calibration of the system as long as all the fiber gratings experience the same thermal variation. Using schemes as the proposed one, progress can be made in little explored applications of reflectometry, such as in the determination of dimensional parameters of mechanical parts (including profilometry of surfaces or parts) and tomography for the study of transparent and semitransparent materials (glass, plastics, polymers, etc.) of large dimensions.

Acknowledgements

This work has been funded by the Consejo Nacional de Investigaciones Científicas y Técnicas (CONICET) (PIP 112-201101-00397), Facultad de Ingeniería de la Universidad Nacional de la Plata (Proyecto I169), Comisión de Investigaciones Científicas de la Provincia de Buenos Aires CIC (Resoluciones N° 1266/14, 602/16, 195/17), and Facultad Regional Delta, Universidad Tecnológica Nacional (PID 2221), Argentina.

Author details


Nélide A. Russo^{1*}, Eneas N. Morel², Jorge R. Torga² and Ricardo Duchowicz¹

¹ Centro de Investigaciones Ópticas (CONICET-CIC), La Plata, Buenos Aires, Argentina

² Laboratorio de Optoelectrónica y Metrología Aplicada, Facultad Regional Delta, UTN, Campana, Buenos Aires, Argentina

*Address all correspondence to: nelidar@ciop.unlp.edu.ar

IntechOpen

© 2020 The Author(s). Licensee IntechOpen. Distributed under the terms of the Creative Commons Attribution - NonCommercial 4.0 License (<https://creativecommons.org/licenses/by-nc/4.0/>), which permits use, distribution and reproduction for non-commercial purposes, provided the original is properly cited. 

References

- [1] Huang D, Swanson EA, Lin CP, Schuman JS, Stinson WG, Chang W, et al. Optical coherence tomography. *Science*. 1991;**254**:1178-1181
- [2] Tearney GJ, Boppart SA, Bouma BE, Brezinski ME, Weissman NJ, Southern JF, et al. Scanning single-mode fiber optic catheter-endoscope for optical coherence tomography. *Optics Letters*. 1996;**21**:543-545
- [3] Hee MR, Izatt JA, Swanson EA, Huang D, Schuman JS, Lin CP, et al. *Archives of Ophthalmology*. 1995;**113**: 325
- [4] Fercher AF, Hitzenberger CK, Kamp G, El-Zaiat SY. Measurement of intraocular distances by backscattering spectral interferometry. *Optics Communication*. 1995;**117**:43-48
- [5] Lexer F, Hitzenberger CK, Fercher AF, Kulhavy M. Wavelength-tuning interferometry of intraocular distances. *Applied Optics*. 1997;**36**:6548-6553
- [6] Häusler G, Lindner MW. 'Coherence radar' and 'spectral radar'—New tools for dermatological diagnosis. *Journal of Biomedical Optics*. 1998;**3**:21-31
- [7] Boppart SA, Tearney GJ, Bouma BE, Southern JF, Brezinski ME, Fujimoto JG. Noninvasive assessment of the developing *Xenopus* cardiovascular system using optical coherence tomography. *Proceedings of the National Academy of Sciences of the United States of America*. 1997;**94**: 4256-4261
- [8] Rogowska J, Bryant CM, Brezinski ME. Cartilage thickness measurements from optical coherence tomography. *Journal of the Optical Society of America*. A. 2003;**20**:357-367
- [9] Walecki W, Suchkov V, Van P, Lai K, Pravdivtsev A, Mikhaylov G, et al. Non-contact fast wafer metrology for ultra-thin patterned wafers mounted on grinding and dicing tapes. In: *IEEE/CPMT/SEMI 29th International Electronics Manufacturing Technology Symposium*. 2004. pp. 323-325
- [10] Walecki WJ, Lai K, Pravdivtsev A, Souchkov V, Van P, Azfar T, et al. Low-coherence interferometric absolute distance gauge for study of MEMS structures. *Proceedings of SPIE*. 2005; **5716**:182-188
- [11] Guss G, Bass I, Hackel R, Mailhiot C, Demos SG. High-resolution 3-D imaging of surface damage sites in fused silica with optical coherence tomography. *Proceedings of the SPIE* 6720; 2007. 67201F
- [12] Walecki W, Wei F, Van P, Lai K, Lee T, Lau SH, et al. Interferometric metrology for thin and ultra-thin compound semiconductor structures mounted on insulating carriers. In: *CS Mantech Conf*. 2004
- [13] Markl D, Hanneschlaeger G, Leitner M, Sacher S, Koller D, Khinast J. A device and a method for monitoring a property of a coating of a solid dosage form during a coating process forming the coating of the solid dosage form. GB application 2513581 (A), EP application 2799842 (A1), US application 020140322429 (A1); 2014
- [14] Walecki WJ, Szondy F. Fiber optics low-coherence IR interferometry for defense sensors manufacturing. In: *Proceeding of SPIE*; 7322; 2009. p. 73220K
- [15] Dufour ML, Lamouche G, Detalle V, Gauthier B, Sammut P. Low-coherence interferometry, an advanced technique for optical metrology in industry. *Insight-Non-Destructive Testing and Condition Monitoring*. 2005;**47**:216-219

- [16] Dufour ML, Lamouche G, Vergnole S, Gauthier B, Padioleau C, Hewko M, et al. Surface inspection of hard to reach industrial parts using low-coherence interferometry. *Proceedings SPIE*. 2006; **6343**:63431Z
- [17] Song S, Xu J, Wang RK. Long-range and wide field of view optical coherence tomography for in vivo 3D imaging of large volume object based on a kinetic programmable swept source. *Biomedical Optics Express*. 2016;**7**: 4734-4748
- [18] Leitgeb R, Hitzenberger CK, Fercher AF. Performance of Fourier domain vs. time domain optical coherence tomography. *Optics Express*. 2003;**11**:889-894
- [19] Chinn R, Swanson EA, Fujimoto JG. Optical coherence tomography using a frequency-tunable optical source. *Optics Letters*. 1997;**22**:340-342
- [20] Bonesi M, Minneman MP, Ensher J, Zabihian B, Sattmann H, Boschert P, et al. A kinetic all-semiconductor programmable swept source at 1550 nm and 1310 nm with centimeters coherence length. *Optics Express*. 2014; **22**:2632-2655
- [21] Huber R, Wojtkowski M, Fujimoto JG. Fourier domain mode locking (FDML): A new laser operating regime and applications for optical coherence tomography. *Optics Express*. 2006;**14**: 3225-3237
- [22] Insight, Akinetic All-Semiconductor Technology. 2016. Available from: <http://www.sweptlaser.com/high-speed-sweeping>
- [23] Huber R, Wojtkowski M, Taira K, Fujimoto JG, Hsu K. Amplified, frequency swept lasers for frequency domain reflectometry and OCT imaging: Design and scaling principles. *Optics Express*. 2005;**13**: 3513-3528
- [24] Huber R, Adler DC, Fujimoto JG. Buffered Fourier domain mode locking: Unidirectional swept laser sources for optical coherence tomography imaging at 370,000 lines/s. *Optics Letters*. 2006; **31**:2975-2977
- [25] Adler DC, Huber R, Fujimoto JG. Phase-sensitive optical coherence tomography at up to 370,000 lines per second using buffered Fourier domain mode-locked lasers. *Optics Letters*. 2007;**32**:626-628
- [26] Huang SW, Aguirre AD, Huber RA, Adler DC, Fujimoto JG. Swept source optical coherence microscopy using a Fourier domain mode-locked laser. *Optics Express*. 2007;**15**:6210-6217
- [27] Huber R, Adler DC, Srinivasan VJ, Fujimoto JG. Fourier domain mode locking at 1050 nm for ultrahigh-speed optical coherence tomography of the human retina at 236,000 axial scans per second. *Optics Letters*. 2007;**32**: 2049-2051
- [28] Iiyama K, Wang LT, Hayashi KI. Linearizing optical frequency sweep of a laser diode for FMCW reflectometry. *Journal of Lightwave Technology*. 1996; **14**:173-178
- [29] Grulkowski I, Liu JJ, Potsaid B, Jayaraman V, Jiang J, Fujimoto JG, et al. High-precision, high-accuracy ultralong range swept-source optical coherence tomography using vertical cavity surface emitting laser light source. *Optics Letters*. 2013;**38**:673-675
- [30] Eigenwillig CM, Biedermann BR, Palte G, Huber R. K-space linear Fourier domain mode locked laser and applications for optical coherence tomography. *Optics Express*. 2008;**16**: 8916-8937
- [31] Bradu A, Neagu L, Podoleanu A. Extra long imaging range swept source optical coherence tomography using re-

- circulation loops. *Optics Express*. 2010; **18**:25361-25370
- [32] Morel EN, Russo NA, Torga JR, Duchowicz R. Interferometric system based on swept source optical coherence tomography scheme applied to the measurement of distances of industrial interest. *Optical Engineering*. 2016;**55**: 014105
- [33] Morel EN, Russo NA, Torga JR, Duchowicz R. Application of a long-range swept source optical coherence tomography-based scheme for dimensional characterization of multilayer transparent objects. *Optical Engineering*. 2017;**56**:084102
- [34] Cerrotta S, Morel EN, Torga JR, Alvira FC. Feasibility and analysis of a system of two in tandem interferometers for optical coherence tomography. In: XVII Workshop on Information Processing and Control (RPIC). 2017. ISSN: 0018-9219
- [35] Antonacci J, Morel EN, Torga JR, Duchowicz R. Spectral sensor resolution measurement improvements by temporal analysis. In: XVII Workshop on Information Processing and Control (RPIC). 2017 ISSN: 0018-9219
- [36] Sallese MD, Morel EN, Tabla PM, Torga JR. Reduction of measurement errors in OCT scanning. *Proceeding of SPIE*. 2018. ISSN: 1605-7422-e-ISSN: 2410-9045
- [37] Cerrotta S, Morel EN, Alvira FC, Torga JR. Large axial range frequency-domain optical low coherence interferometry. *IEEE Photonics Technology Letters*. 2019;**31**:125-128
- [38] Giordana A, Duchowicz R. Development and analysis of a simple tunable erbium ring laser. *Proceedings of SPIE*. 2011;**8011**:80115A
- [39] Kashyap R. *Fiber Bragg Gratings*. 2nd ed. USA: Academic Press—Elsevier; 2009
- [40] Othonos A, Kalli K. *Fiber Bragg Gratings: Fundamentals and Applications in Telecommunications and Sensing*. Artech House: USA; 1999
- [41] Yun SH, Richardson DJ, Kim BY. Interrogation of fiber grating sensor arrays with a wavelength-swept fiber laser. *Optics Letters*. 1998;**23**:843-845
- [42] Oppenheim AV, Schafer RW. *Discrete-Time Signal Processing*. 2nd ed. Upper Saddle River, New Jersey, USA: Prentice-Hall; 1998
- [43] Na J, Choi WJ, Choi ES, Ryu SY, Lee BH. Image restoration method based on Hilbert transform for full-field optical coherence tomography. *Applied Optics*. 2008;**47**:459-466